k-Space-Based Enhancement of Pulmonary Hyperpolarized ^{129}Xe Ventilation Images

He Deng, Caohui Duan, Sa Xiao, Junshuai Xie, Huiting Zhang, Xianping Sun, and Xin Zhou

Abstract—Hyperpolarized (HP) noble gas (e.g., ^{3}He/^{129}Xe) MR images are susceptible to noise and artifacts due to the rapid attenuation of nonrenewable HP magnetization along with the scan time. However, a little attention is paid to this issue through postprocessing techniques. Here, a k-space-based analysis method is proposed to improve the overall signal-to-noise ratio (SNR) and lessen the blurring of pulmonary HP ^{129}Xe ventilation images. This method performs k-space weighting using low-frequency boost and a high-frequency modulation which offsets the magnetization loss per excitation, and then integrates two outputs in image domain through a convex combination model. Furthermore, a nonreference quality metric, called second-derivative measure of improvement by entropy (SMIE), is introduced to assess the image quality of HP gas MRI. The simulation results demonstrate that the enhanced images are statistically significantly different to the original ones regarding the SNR, peak SNR, structural similarity, and SMIE (each P-value is less than 0.0001). *In vivo* results indicate that the proposed method significantly upsets the SNR and SMIE in human pulmonary HP ^{129}Xe ventilation images (all P-values are less than 0.05), while maintaining the appearance of ventilation defects or fine structures. In this case, the proposed scheme has potential for improving the understandability and/or differentiation of regions of interest in the lung.

Index Terms—^{129}Xe, hyperpolarized (HP) gas, image enhancement, k-space, magnetic resonance imaging.

I. INTRODUCTION

LUNG cancer was accounted for 17.09% of all new cancers and 21.68% of all cancer deaths in 2015 in China, which indicates that lung cancer is the most common incident cancer and the leading cause of cancer death in China [1]. Inadequate prevention, few screening chances, and lack of early diagnosis are the major causes of high incidence and low five-year survival rate [2]. Accordingly, early detection and diagnosis are crucial to decreasing cancer mortality, especially

for stage-I lung cancer [2]. At present, pulmonary function tests (PFTs), chest X-rays, and computed tomography (CT) are the most commonly used techniques for pulmonary disease diagnosis. Nevertheless, such techniques are incapable of offering overall lung microstructure parameters, and/or local-regional gas–gas/gas–blood exchange functions [3]. Nevertheless, early signs of pulmonary diseases are characterized by the changes in lung functions [4]. Moreover, both the chest X-rays and CT are limited by the radiation of X-ray. Consequently, there is a strong demand to move beyond form to function in lung imaging.

Hyperpolarized (HP) noble gasses (e.g., ^{129}Xe or ^{3}He) MRI is a powerful noninvasive facility for quantitatively discerning lung structures and gas-exchange functions [5]–[10]. Using HP gasses, MR signals in the airspaces of the lung are amplified up to 10^3–10^5 times above the thermal equilibrium levels, which makes imaging of lung ventilation or diffusion possible [11]. Howbeit, such nonequilibrium polarization is nonrenewable, which leads to the rapid attenuation of available HP magnetization along with each excitation pulse [12]. Thus, it is difficult to simultaneously obtain high signal-to-noise ratio (SNR) and spatial resolution of HP MR images. Moreover, the magnetic susceptibility artifacts at the air–tissue interfaces and motion artifacts because of the respiration and cardiovascular pulsation potentially distort and degenerate HP images [10]. In addition to the above factors, the limitations of MRI hardware systems (such as inhomogeneity of magnetic field and coil sensitivity) and unavoidable diverse kinds of noise (e.g., signal-dependent and non-Gaussian noise) further deteriorate the image quality. Accordingly, HP gas MR images potentially have heavy noise, artifacts, low resolution, or poor contrast, which brings great difficulties in diagnosing lung diseases. Accurate or precise diagnoses need smart strategies to enhance the quality of images.

Up to date, the techniques to improve HP gas MR images are roughly classified into two categories. The first focuses on the hardware updates [10], such as the development of the polarizer and the use of multichannel coils. Nevertheless, the continued improvements in polarization levels and available volumes per unit time need innovations in hardware/software configurations. The second category takes into account the reformations of the signal acquisition speed, e.g., the usage of fast pulse sequences, parallel imaging [12], small-angle excitation [13], along with undersampling strategies [14], aiming to acquire more data or shorten breath holding time [4]. Nevertheless, the breath-hold imaging of HP gas faces unique challenges that can ultimately achieve different acquisition tactics [15]. In general, the above

pay little attention to the use of postprocessing methods (such as image denoising or enhancement), although such algorithms are generally adopted to improve the image quality in the MR field [16]–[18]. Thus, we take into account the use of postprocessing algorithms, aiming to improve the visualization of regions of interest (ROIs) in pulmonary HP [129]Xe MR images (including SNR and fine-structural details of the lung) without impacting the acquisition process or hardware costs.

An image signal could be thought of as a sum of a distortion-free reference signal and an error signal. Fewer errors result in a higher quality image. There are a lot of simple and well-studied postprocessing algorithms to improve the image quality (or lessen error signals), e.g., the median filtering (MDF), block-matching and 3-D filtering (BM3D) [19], fast iterative shrinkage and/or thresholding filtering (FISF) [20], fast bilateral filtering (FBF) [21], and trilateral filtering [22]. The MDF technique is known due to its outstanding performance at removing salt and pepper noise, while its usage is hindered by the algorithmic complexity, nonlinearity, and nonseparability [23]. The BM3D generates the state-of-the-art performance in denoising. Nevertheless, many parameters are included in BM3D, and it will be difficult to find optimal ones. The FISF basically considers the local correlation among image pixels for denoising or deblurring problems [24], while neglecting the sparsity of signals. The FBF strategy is an edge-preserving diffusion filtering tool, but the computational complexity depends on its filtering kernel size [21]. Different from the above algorithms (performed in image domain rather than frequency domain), apodization (or line broadening) simplifies the spectrum for improving the visualization of resonances while filtering high-frequency noise [25], which is usually achieved with a Lorentzian function for the *k*-space center and the Gaussian function for the edges. Nevertheless, this smoothes noise, while does so at the expense of creating wider signals [26].

Since MR signals are sampled during the usage of the magnetic encoding gradient, it involves the spatial-frequency distribution (viz., *k*-space) of the sample. The *k*-space center comprises low spatial-frequency information of the sample and determines the overall SNR and contrast of the image [27]. On the other hand, high spatial-frequency components acquired further away from the *k*-space center contribute to the image edges, details, and/or sharpness. The actual HP MR image information is achieved using the fast Fourier transform (FFT) of the sampled data, as shown in Fig. 1. It can be seen that the image SNR and contrast depend upon the signal magnitude in the low spatial-frequency regions of the *k*-space [see Fig. 1(b)], but the resolution is related to the maximum spatial-frequency gained [see Fig. 1(c)]. Howbeit, a little attention is paid to the enhancement of HP gas MR images according to these *k*-space properties.

This paper is concentrated on the *k*-space analysis for postprocessing pulmonary HP MR images (centric the Cartesian rather than radial or spiral acquisition). We find that original *k*-space could reproduce the raw data if multiplied by a weighting (or coefficient) matrix (all weights in this case are: 1) if we amplify the weights in the low spatial-frequency region of *k*-space (viz., the k-space center), an SNR-weighted
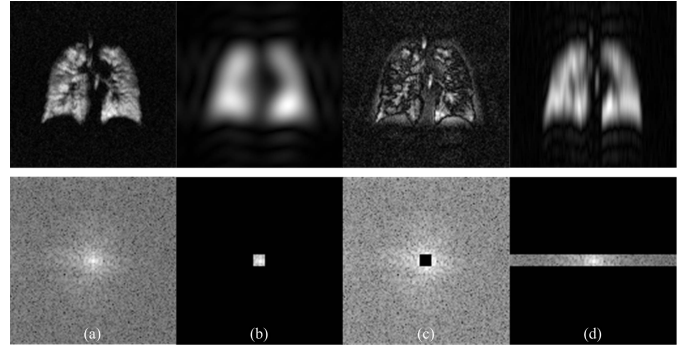

Fig. 1. One slice of the pulmonary HP [129]Xe images (upper) of a COPD patient (female, age 56, scanned by 1.5 T · S) and their associated *k*-space data (lower). (a) Full data set. (b) *k*-space center contains low spatial frequencies, determining the overall image contrast, brightness, and general shapes. (c) *k*-space periphery comprises high spatial frequencies, dominating image edge, details, and sharp transitions. (d) Narrow *k*-space band provides high resolution along its length and low resolution perpendicular or along its width.

result will be obtained. Similarly, the adjustment of weights in the periphery of *k*-space yields a resolution-weighted result. Different from line broadening, these are separately performed in the *k*-space domain. After that, an enhanced result is achieved by fusing the SNR- and resolution-weighted results (in the image domain), manipulating the tradeoff between the SNR and fine details. With these considerations in mind, we construct a novel *k*-space-based enhancement method through the *k*-space manipulations (*k*-space weighting matrices) to visually enhance the pulmonary HP gasses ventilation images. This is straightforward and easily implemented, without additional cost and/or preparation. Furthermore, owing to the absence of reference image, we introduce a new blind quality metric of HP MR image, namely, second-derivative measure of improvement by entropy (SMIE). The performance of the proposed algorithm is demonstrated by simulation and *in vivo* experimental results and is quantitatively evaluated using the SNR and SMIE terms. Besides, the effects of the proposed method are validated by the comparisons with baseline filtering algorithms regarding noise and artifact reduction and fine-structural preservation.

The rest of this paper is organized as follows. In Section II, we explain the *k*-space-based enhancement method of HP gas images in detail. In Section III, we give extensive experimental results and discussions. Conclusion and perspectives are given in Section IV.

II. ENHANCEMENT OF PULMONARY HP GAS MR IMAGE

In this section, we describe a scheme for postprocessing HP [129]Xe MR images with the aim of increasing the overall SNR as well as lessening image blurring caused by the decay of HP magnetization over time owing to repeated radio frequency (RF) excitation. This scheme decomposes *k*-space data into low-/high-frequency components, then adopts different *k*-space weighting matrices to improve either SNR or resolution of HP gas images (Fourier linear filtering in effect: the SNR improvement by high weighting in the *k*-space center while resolution improvement from high weighting in the *k*-space periphery). After that, the two output results are integrated through fusion operators in image domain.

A. SNR Improvement

SNR and resolution are the key parameters to quantitatively evaluate MR images. Usually, increasing the scanning time in MR imaging can improve the SNR, resolution, or both [28], but this does not work in HP gas MRI due to the nonrenewability of HP magnetization [13]. In fact, the set of MR signals used to fill k-space are discretely sampled, and then constructs a finite k-space matrix. Once given the matrix, the SNR and resolution are subsequently determined. If raw sampled data are properly regulated without boosting/generating artifacts/noise, the SNR and fine structures of the lung are possibly improved to fulfil, especially requirements in applications. This can be done through specific weighting matrices. Assume that a raw k-space matrix S is multiplied by a weighting matrix C, that is,

$$K = S \odot C \tag{1}$$

where K denotes the regenerative k-space data, and $\odot$ denotes the element-wise (Hadamard) product. The matrices K, C, and S have the same dimensions. If C is a matrix of ones, K is equal to S. For specific applications, the designation of elements in the weighting matrix is an important issue.

As stated previously, the image SNR of HP MRI depends on the signal magnitude in the k-space center [13]. Suppose (u_0, v_0) is a middle point in a given k-space, the central region could be defined as

$$\Omega = \{(u, v) | \max(|u - u_0|, |v - v_0|) \le h\} \tag{2}$$

where h is a positive integer that regulates the window size. The trajectory of points in Ω is a square. If we expect the data in the central region to be magnified, without impacting other points (viz., high weighting in the k-space center), a coefficient matrix C_1 is founded as follows:

$$C_1 = \begin{cases} \beta, & \text{if } (u, v) \in \Omega \\ 1, & \text{else} \end{cases} \tag{3}$$

where β is a constant (usually greater than 1). After that, (1) becomes $K_1 = S \odot C_1$. After FFT, an image $f_1(x, y)$ is constructed by the following formula:

$$
\begin{aligned}
f_1(x, y) &= \frac{1}{NM} \sum_{u=0}^{N-1} \sum_{v=0}^{M-1} K_1(u, v) e^{j2\pi(ux/N + vy/M)} \\
&= \frac{1}{NM} \left[\sum_{(u,v) \in \Omega} \beta S(u, v) e^{j2\pi\left(\frac{ux}{N} + \frac{vy}{M}\right)} \right. \\
&\quad \left. + \sum_{(u,v) \notin \Omega} \beta S(u, v) e^{j2\pi\left(\frac{ux}{N} + \frac{vy}{M}\right)} \right] \\
&= \frac{1}{NM} \left[\sum_{(u,v) \in \Omega} \beta |S(u, v)| e^{j2\pi\left(\frac{ux}{N} + \frac{vy}{M} - \phi\right)} \right. \\
&\quad \left. + \sum_{(u,v) \notin \Omega} \beta |S(u, v)| e^{j2\pi\left(\frac{ux}{N} + \frac{vy}{M} - \varphi\right)} \right]
\end{aligned} \tag{4}
$$

where the size of the k-space matrix is $N \times M$. In this case, the signal magnitudes inside the k-space center are amplified

by β times, without impacting high spatial-frequency data. Since the noise distribution of an MR image is Rician (values cannot be less than 0), we adopt the following formula to calculate SNR:

$$\text{SNR} = \frac{\text{mean(Signal)} - \text{mean(Noise)}}{\text{stdev(Noise)}} \tag{5}$$

where stdev denotes the standard deviation. In this case, (5) would account for the increasing of noise floor across the entire image. Therefore, the mean signal intensity ascends, while the mean and stdev of noise change slightly although boosting the low spatial-frequency components also possibly amplifies low spatial-frequency noise. This raises SNR values.

In SNR calculation, signal regions are determined through an iterative threshold [29], and noise voxels are sampled from all regions of the image outside of the lung. If the parameter in (3) is given, the window size will be related to SNR of MR images. (The weighting matrix is an array of 1's except for a square of side length $2h$). We rewrite (3) as follows:

$$C_1 = C_2 + 1, \quad \text{where } C_2(u, v) = \begin{cases} \beta - 1, & \text{if } (u, v) \in \Omega \\ 0, & \text{else} \end{cases} \tag{6}$$

where C_2 is a rectangle function, and 1 is a matrix of 1's. Then, (1) turns into $K_1 = S \odot C_2 + S$. In MRI, the field of view (FOV) and the spacing between the samples (i.e., k) in the k-space are in inverse proportion, specifically, $\Delta k = 1/\text{FOV}$. This relationship keeps between the pixel width ($\Delta\omega$) and the range between the highest positive and negative spatial frequencies of k-space (denoted by k_{FOV}). The expression $S \odot C_2$ is considered that the data sampling rate and spacing remain the same, reducing k_{FOV} by a factor (a function of h). For example, if the factor is set to 1/4, with this k-space multiplication, FOV stays the same, but the pixel width has been tripled from 1 to 4 mm. The larger pixel size could yield lower spatial resolution of image. In this case, the multiplying of the window function [e.g., (3)] will lose resolution of an image, which is hard to retrieve in practice. Therefore, the window function is a tradeoff between SNR and resolution improvements.

B. Resolution Improvement

Since C_1 could be seen as a window (rectangle) function, the multiplying of a rectangle function in the k-space will definitely lose image resolution. In addition, the centric-phase-encoding strategy can cause a loss of high spatial-frequency information because of rapid depletion of nonrenewable HP magnetization [27]. To offset such loss, a weighting matrix whose periphery has large weights is founded (that is, high weighting along the k-space periphery). Suppose that the size of the k-space matrix is $N \times M$ (where N is along the frequency encoding direction while M is along the phase-encoding direction), the coefficient matrix C_3 is defined as

$$C_3(r, :) = \begin{cases} \cos^{-2(M/2 - r)}\theta, & \text{if } r \in [1, M/2] \\ \cos^{-2(r - M/2) + 1}\theta, & \text{else} \end{cases} \tag{7}$$

where r is the index of the phase-encoding direction, and θ is within the interval $[2°, 10°]$. As distinct from matrix C_1, the weights in the periphery of C_3 are greater than 1, while in the central lines are almost 1. Hence, (1) turns into $K_2 = S \odot C_3$, whose aim is to compensate for the flip angle and decay losses across phase encodes. Nevertheless, matrix C_3 magnifies the signal intensities of the edge but amplifies some disadvantages (e.g., artifacts and noise) at the same time. Furthermore, the choice of weighting enhancement over a box possibly introduces ringing artifacts. Thus, we use BM3D [19] to eliminate unfavorable factors. After FFT, a resolution-weighted image is obtained.

To select an appropriate parameter in (7), a local contrast metric (LCM) is defined as

$$\text{LCM}^k = -20 \cdot \log\left(1 - \frac{2}{q^k + 1}\right)$$

where

$$q^k = \frac{J_{\max}^k - J_{\min}^k}{J_{\max}^k + J_{\min}^k} \tag{8}$$

where the image is divided into k nonoverlapping blocks, and $J_{\max}^k$ and $J_{\min}^k$ are the maximum and minimum intensities of the kth block. The average of LCM is calculated. For the sixth and seventh slices of pulmonary HP ^{129}Xe images of the chronic obstructive pulmonary disease (COPD) subject, the curves of average LCM under different thetas are shown in Fig. 2(a) and (b), where the number of blocks is 100, and theta is in the internal $(2°, 42°)$. It can be found that the curves have large value in the range of $2°$–$10°$, declines rapidly in an interval $[10°, 15°]$, and then keeps relatively steady low levels in other scopes. This phenomenon possibly has to do with some characters of an image (e.g., visual quality). The respective resolution-weighted images of the seventh slice of the lung are shown in Fig. 2(c)–(e), when θ in (7) is set to $7°$, $12°$, and $17°$. It can be found that the degree of residual noise and artifacts is involved in the average LCM values (in the inverse ratio). Low value possibly results in heavy noise and/or artifacts, especially for Fig. 2(e), where the lung signals are concealed by the heavy noise and artifacts. This may supply guidance in selecting parameter θ in (7). For example, we utilize the maximum of average LCM that defines an optimum of parameter θ or other reasonable strategies [such as θ could be set to $\arctan(\text{sqrt}(1/(M-1)))$, where M denotes the total number of excitation].

C. Fusion

From the above, SNR-weighted results improve the SNR and coarse features while sacrificing fine details [see Fig. 3(a)]. On the other hand, resolution-weighted results are able to highlight fine features of ROIs [see Fig. 3(b)]. If the weighting functions are applied in k-space simultaneously, and 2-D FFT is performed only once, the SNR and structural details are potentially poorer than the original [see Fig. 3(d)]. Consequently, we perform the fusion in image domain, that is, SNR- and resolution-weighted results are integrated to achieve an
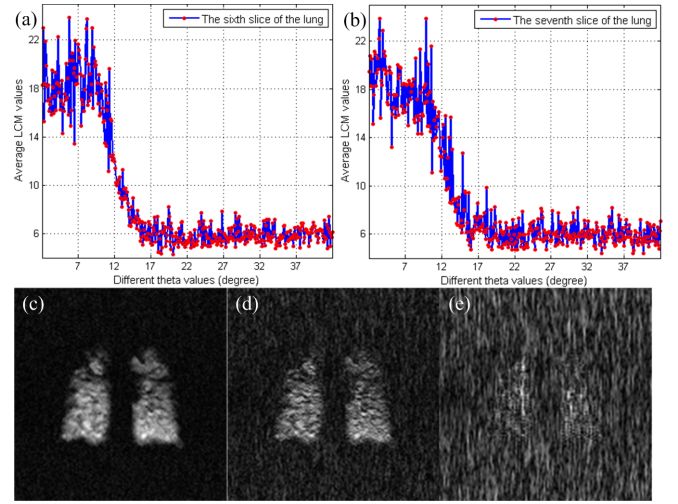

Fig. 2. (a) and (b) For the sixth and seventh slices of the COPD subject, the changing curve of average LCM under diverse theta values. (c)–(e) Resolution-weighted images of the seventh slice of the lung, when parameter θ in (7) is set to $7°$, $12°$, and $17°$, respectively.
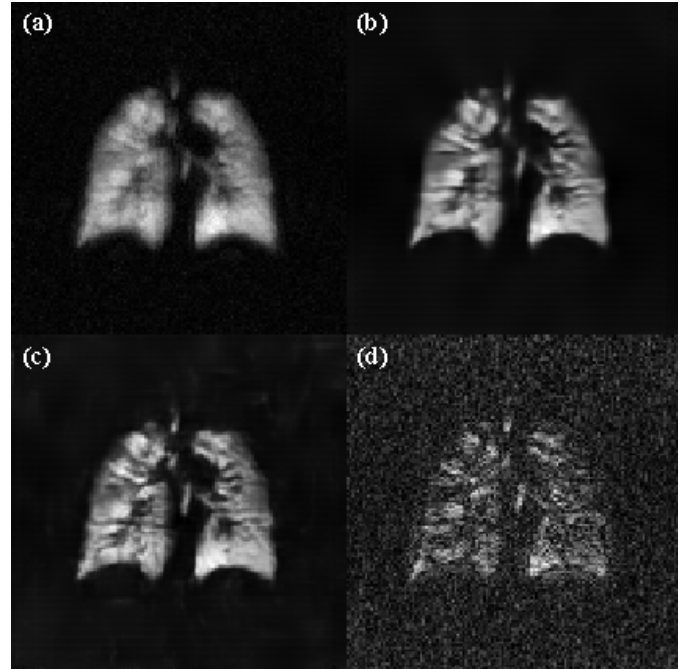

Fig. 3. For Fig. 1(a), the comparison by separately or simultaneously weighting the center and edges of k-space. (a)–(c) SNR-weighted, resolution-weighted, and enhanced results obtained using (3), (7), and (9), respectively. (d) Reconstructed result by manipulating the weighting of the center and edges of k-space simultaneously.

enhanced result F [see Fig. 3(c)], that is,

$$F(m, n) = \alpha \cdot \frac{F_1(m, n)}{|F_1|_{\max}} \oplus (1 - \alpha) \cdot \frac{F_2(m, n)}{|F_2|_{\max}} \tag{9}$$

where F_1 and F_2 are the SNR- and resolution-weighted results, $|F_1|_{\max}$ and $|F_2|_{\max}$ are the corresponding maximum absolute values, $\oplus$ is the element-wise (arithmetic) addition, and α is the scaling factor, respectively.

The convex combination model presents a tradeoff between the overall SNR and fine details of images. We seek an optimal

value of scalar parameter, which combines those corresponding to abundant local features. Since local entropy represents the local information contained in a patch (or characterizes topographic features of an image), we choose an optimum α that results in the minimum variation of local entropy values across patches. Let $U_t(\alpha)$ be the local entropy of the tth patch (Ω_t) of an enhanced result obtained through (9), and $\overline{U}(\alpha)$ is the average value of local entropy across all patches. The optimum α is searched by settling the following optimization problem, which could be solved numerically:

$$\alpha^* = \arg\min_{0 \leq \alpha \leq 1} \sum_t (U^t(\alpha) - \overline{U}(\alpha))^2$$

where

$$U^t(\alpha) = -\sum_{s_i \in \Omega_t} p(s_i)\log p(s_i) \qquad (10)$$

where $p(s_i)$ is the probability distribution at the point s with the ith intensity level.

D. Nonreference Metric

Most objective/quantitative metrics of the image quality require a reference (viz., distortion free) image that is assumed to have perfect quality [29]. However, such metrics is unsuitable for HP gas MRI owing to the lack of reference image. Nevertheless, nonreference or blind quality criterion is absent for quantitatively evaluating HP gas MR image. Thus, we introduce a novel blind quality metric (SMIE) to evaluate the image quality of HP MRI, which is derived from the concept of the second-derivative-like visibility operator and virtues of some earlier reviewed indexes [31]–[33]. The SMIE is defined as

$$\text{SMIE}_{s \times t} = -\frac{1}{s \times t} \sum_{x=1}^{s} \sum_{y=1}^{t} \omega\rho^{\omega}\ln\rho$$

$$\text{where} \quad \rho = \frac{|I_{\max} - 2I_{\text{med}} + I_{\min}|}{|I_{\max} + 2I_{\text{med}} + I_{\min}|} \qquad (11)$$

where an image I is divided into the sequential $s \times t$ blocks. (Each block has the same size. In this paper, we set $s = t = 10$.) $I_{\max}$, I_{med}, and $I_{\min}$ are the maximum, median, and minimum intensities in every block, and ω is a positive constant. After that, the average of measurement results of all blocks in the entire image is calculated as a quality measure. For the kth block, $I_{\text{med}}^k \neq 1/2(I_{\max}^k + I_{\min}^k)$ because of the SMIE definition, therefore, the blocks with $I_{\text{med}}^k = 1/2(I_{\max}^k + I_{\min}^k)$ are abandoned when computing the SMIE of an image (because the SMIE value will approach infinity). If $I_{\text{med}}^k = 0$ for all blocks, the minimal SMIE value is 0.

Since $I_{\max}^k$, I_{med}^k, and $I_{\min}^k$ in (11) are not less than 0, the variable ρ is within the range of [0, 1]. Considering a function

$$f(\rho) = \int h(\rho)d\rho, \quad \text{where } h(\rho) = -\omega\rho^{\omega}\ln\rho. \qquad (12)$$

The first derivative of $h(\rho)$ is $g(\rho) = -\omega\rho^{\omega-1}(\omega\ln\rho + 1)$. Suppose that $\rho_0 = e^{-1/\omega}$, then $g(\rho) > 0$, if $\rho \in (0, \rho_0)$ and

$g(\rho) < 0$, if $\rho \in (\rho_0, 1)$. Thus, $[\rho_0, f(\rho_0)]$ is an inflection point of the function $f(\rho)$. If $0 < \omega \leq 1$, the function $h(\rho)$ rapidly reaches the maximum $1/\omega e$, and then decreases to 0 at relatively slow speed. On the other hand, if $\omega > 1$, the function $h(\rho)$ slowly expands to the maximum, and then slowly decreases to the minimum. The properties offer the instruction on reasonably choosing parameter ω in (11). For example, in order to avoid confusion (different values of ρ may result in the same function value), parameter ω could be reasonably selected in the range of 0–0.5 (or smaller range) in specific applications, such as $\omega = 0.2$ in this paper.

III. EXPERIMENTAL RESULTS

In this section, we first introduce simulation and *in vivo* data and baseline methods (e.g., current state-of-the-art denoiser) for comparisons. After that, we use experimental results to test the effectiveness and practicality of the proposed algorithm.

A. Data and Baseline Methods

Simulations are adopted to justify the relevance of SMIE and SNR as reference-free metrics of image quality, and to validate the effects of the proposed method in a simulated environment. The k-space signal acquired by proton (^{1}H) MRI can be used to approximately simulate the k-space data of HP gas MRI with a constant-flip-angle scheme [13]. That is,

$$\hat{A}(p, q) = A(p, q) \cdot \cos^{p-1} \tau \sin \tau + A_n \qquad (13)$$

where A and $\hat{A}$ denote the original ^{1}H and simulated HP k-space data, A_n denotes the additive Gaussian noise, (p, q) denotes the spatial pixel index, and τ denotes the small flip angle, respectively. The ^{1}H k-space data of a water phantom acquired on the 1.5 T whole-body MRI Scanner (Avanto, Siemens Medical Solutions) is used to approximately produce the k-space data of HP MRI. The imaging parameters of the phantom were: echo time (TE) = 9.8 ms, TR = 20.0 ms, bandwidth (BW) = 3.2 kHz, matrix size (MS) = 320 × 320, FOV = 52 × 52 mm^2, slick thickness (ST) = 20 mm, and 2-D FLASH sequence. This work had done 100 times (the angle τ was selected as 8°), resulting in the k-space data with a size of 320 × 320 × 100.

After that, human HP ^{129}Xe ventilation images are tested to demonstrate the performance of the proposed algorithm with respect to the improvement of SNR and SMIE, but maintaining the appearance of fine structures and ventilation defects. Three healthy volunteers (average age, 24 years), two patients with asthma (34 years) or COPD (56 years) were enrolled for HP ^{129}Xe MRI experiments after provided informed consents. All experiments were approved by the Institutional Review Board, Wuhan Institute of Physics and Mathematics, Chinese Academy of Sciences, Wuhan, China. Experiments were performed on a 1.5-T scanner (Siemens) using a homebuilt transmit–receive vest RF coil. Enriched xenon was polarized using the spin-exchange optical pumping with a "freeze-out" accumulation procedure in a cold finger and a home-built xenon polarizer. The polarizer was equipped with a 75-W narrow width laser array working in the continuous-flow mode. The source gas mixture consisted of 1% enriched xenon
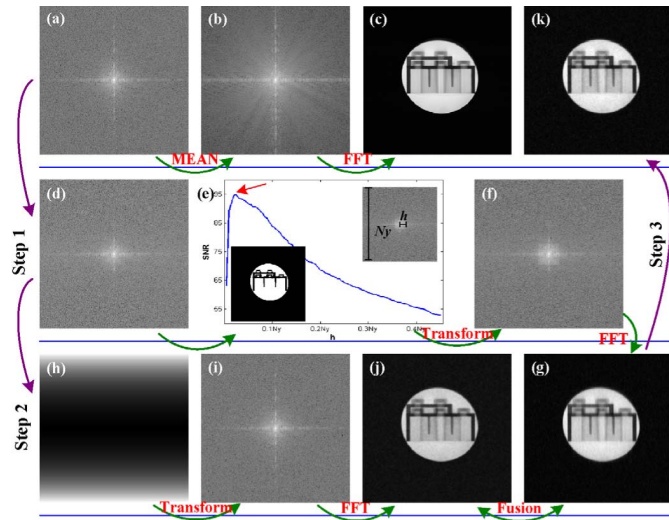
Fig. 4. Comparison images of the water phantom through three different steps. (a) Original ^{1}H k-space of one scan is used to simulate (d) HP k-space data. (b) Average ^{1}H k-space and (c) corresponding reconstructed image are shown as references. Step 1: (e) Relationship between hs and average SNR of SNR-weighted images when β is set to 2, where red arrow denotes an optimal h for maximum SNR (where Ny is the image size). (f) Weighted k-space and (g) SNR-weighted image are constructed. Step 2: (d) Simulated raw k-space is multiplied by (h) weighting matrix using high-frequency modulation, aiming to improve the image resolution. After the FFT followed by BM3D filtering, (j) resolution-weighted image is obtained. Step 3: (g) and (j) Integrating images and (k) enhanced result are achieved.

(86% 129-isotope), 89% ^{4}He, and 10% N_2. Then, the HP gas was extracted into a Tedlar bag from the cold finger just before HP experiments. The available polarization in the bag was approximately 10%–15%. A 500-mL HP xenon and 500-mL medical grade N_2 were mixed to a 1-L gas mixture.

The MRI parameters for the healthy volunteers were: TE = 2.7 ms, TR = 6.8 ms, MS = 128 × 128, FOV = 400 × 400 mm^2, ST = 20 mm, BW = 25.6 kHz, number of slices (NS) = 7, total scan time (TST) = 6.05 s, 2-D bSSFP sequence, constant flip angle [the angle was 70°], and linear encoding. Different from the healthy volunteers, the flip angle used in the asthmatic subject was 50°, while other parameters were the same. For the COPD subject, the NS was 8, TST was 6.92 s, and other imaging parameters remained constant. After the acquisition of the simulated and *in vivo* k-space, the raw data were used to test the proposed method regarding the improvement of image quality. All the groups of data were processed in MATLAB.

Since the proposed k-space weighting metrics belong to the Fourier filtering in effect, we chose some widely used filtering techniques as the baseline methods for comparisons, such as MDF, BM3D [19], FISF [20], and FBF [21]. These algorithms could effectively yield better image quality (e.g., denoising or restoration) in the image domain. A two-tailed Student's *t*-test (two-sample comparison of mean) was performed for statistical comparisons of quantitative metrics (e.g., SNR or SMIE), and a *P*-value < 0.05 was considered as statistically significant.

B. Simulation

For the water phantom, Fig. 4(c) shows the ^{1}H MR image, and its k-space is shown in Fig. 4(b), with 100 averages.

This ^{1}H image is considered to possess high image quality (e.g., high SNR and resolution), and is regarded as the ground truth (viz., reference image in this section). Based on (13), the raw ^{1}H k-space of each scan [e.g., Fig. 4(a)] is applied to simulate HP k-space data [e.g., Fig. 4(d)]. This generates 100 groups of simulated k-space data. After that, the simulated data are utilized to generate SNR-weighted images (through Step 1), resolution-weighted images (through Step 2), and fused results (through Step 3), as shown in Fig. 4.

In Step 1, we search an optimal value of h to maximize the image SNR. We construct the relationship between hs and average SNR of SNR-weighted images (a total of 100) when β is set to 2, as shown in Fig. 4(e). When calculating SNR, the reference image is segmented through an iterative threshold [29], to yield signal regions, and the residue is simply selected as noise areas, as shown in Fig. 4(e). The segmentation threshold is calculated once for the reference image and applied to define the boundary for the modified images. In this case, the signal and noise areas keep the same for different hs or SNR-weighted images. Hence, we obtain an optimized weighted k-space [e.g., Fig. 4(f)]. After FFT, an SNR-weighted image is obtained [e.g., Fig. 4(g)]. In Step 2, the simulated k-space data [e.g., Fig. 4(d)] are multiplied by other weighting matrix [e.g., Fig. 4(h)] whose periphery has high weighting values, to produce a new k-space [e.g., Fig. 4(i)]. Via FFT and BM3D, a resolution-weighted image is produced [e.g., Fig. 4(j)]. In Step 3, the SNR- and resolution-weighted images are fused to generate an enhanced result [e.g., Fig. 4(k)]. Compared with the reference image, the image (k) holds high SNR and accuracy.

The raw ^{1}H k-space data of the water phantom generate 100 groups of simulated HP images (denoted by the original images). Through the proposed postprocessing algorithm, 100 groups of enhanced results are thereupon produced. It is known that a digital image is vulnerable to a wide variety of distortions during the processing, storage, and reproduction, any of which possibly causes a degradation of visual quality. It is necessary to pursue objective image quality metrics to efficiently monitor, judge, or adjust the image quality in applications [31]. The common full-reference quality metric is peak SNR (PSNR) [34], which owns clear physical meanings. Structural similarity (SSIM) [24] is a general quality index to measure the similarity between the reference and processed images. Since there exists a reference image [viz., Fig. 4(c)], we use PSNR and SSIM to evaluate the quality of the original and improved images. Moreover, SNR and SMIE are seen as the two blind image quality criteria.

The upper row in Fig. 5 displays the PSNR, SSIM, SNR, and SMIE comparisons of images without and with the k-space weighting, and the statistical analyses are shown in the lower row. We can see from Fig. 5 that the *P*-value in any comparison is less than 0.0001. This suggests that the improved results are statistically significantly different from the original images in PSNR, SSIM, SNR, and SMIE terms. Moreover, we can see that the evaluation results using SMIE term are consistent with that using two full-reference quality metrics. Consequently, SMIE can be taken as a quantitative measure of image quality improvement provided by the proposed
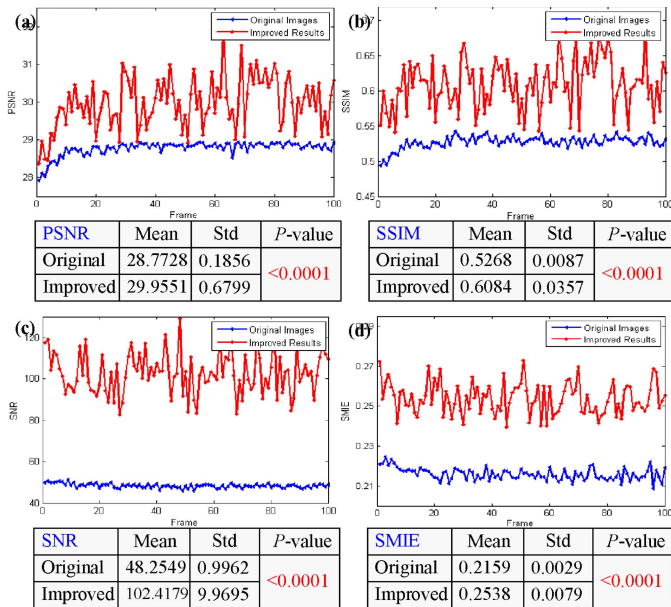
Fig. 5. (a)–(d) PSNR, SSIM, SNR, and SMIE comparisons between the original images and enhanced images obtained using the proposed method for the water phantom (upper), respectively, and their statistical analyses (lower), where original images are artificially synthesized HP images. In SSIM comparisons, the original and modified images are compared with Fig. 4(c) (reference image) rather than the original ones.

postprocessing algorithm. Large SMIE value means a good quality of HP gas images. We can also find that the standard deviation (SD) of all metrics for every increase fluctuates significantly, even when comparing the SD as a percentage of the mean. This means that the proposed k-space weighting way possibly creates much uncertainty and a large distribution of the voxel intensities despite the improved image quality. Probable causes are that the proposed method amplifies the local contrast in the MR images, which expands the range of voxel intensities.

C. In Vivo

The k-space center represents the coarse features of MR image, while its periphery represents fine structures. When the weights of the k-space data are modulated through different coefficient matrices, the coarse or fine characteristics can be adjusted. This is useful to extract ROIs. For a healthy volunteer, Fig. 6 shows one slice of pulmonary HP ^{129}Xe MR images and filtered results obtained using different methods, where red arrows denote the fine structures (such as the trachea or vascular areas). It can be seen that massive artifacts and noise impact the visual quality of the original image [see Fig. 6(a)]. However, through our algorithm, those disadvantages are effectively eliminated, and the overall SNR is increased and fine details are highlighted [see Fig. 6(f)].

Unlike a photograph, CT or X-ray, the contrast in HP gas MR images comes from the microscopic magnetic properties, such as spin density, susceptibility, or partial pressure of HP gasses. This causes some changes of homogeneity or inhomogeneity in ventilated regions (even ventilation defects) after the proposed method. Because there are no ventilation
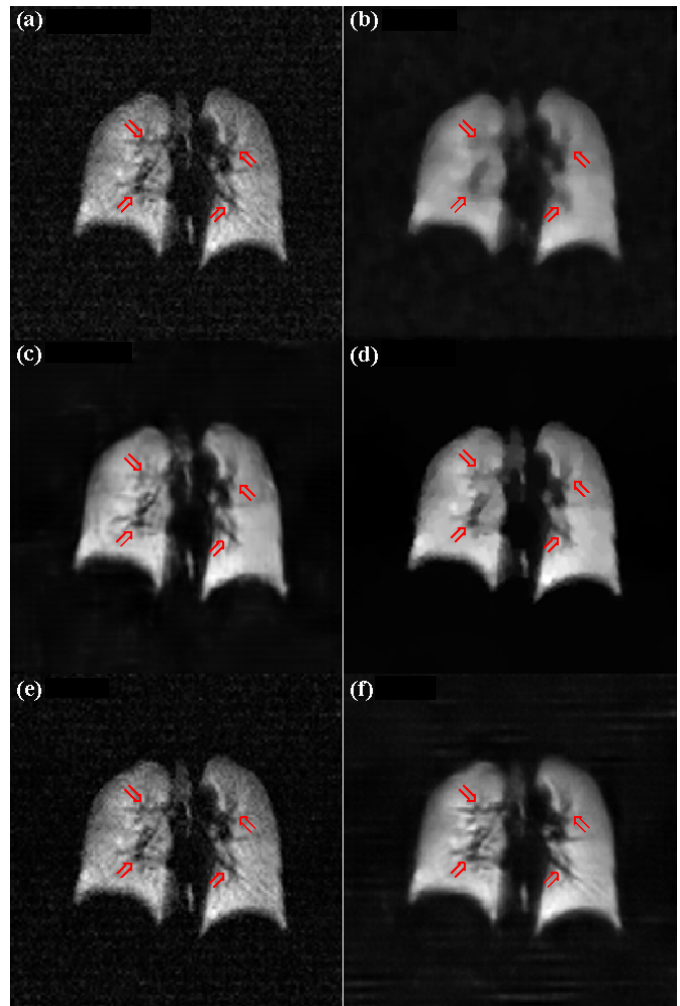

Fig. 6. One slice of the pulmonary HP ^{129}Xe MR images of a healthy volunteer (Healthy 1 shown in Table I, male, 24 years), and filtered results through different algorithms. (a) Original image is filtered through (b)–(f) MDF, BM3D, FISF, FBF, and proposed method, respectively. Red arrows: fine structures.

defects for the healthy subject, the HP gas should disperse homogeneously in the lung. This is the case if one is to expect the exact same amount of HP gas in each voxel. When compared with the original image [viz., Fig. 6(a)], the homogeneities are improved in the image (f).

The filtered results of Fig. 6(a) through the baseline methods are shown in Fig. 6(b)–(e), respectively. We can see that MDF not only causes blocking artifacts but also blurs the fine details, although it can lessen artifacts and/or noise to some extent. BM3D has good denoising performance but blurs fine details to a certain extent. The filtering performance of FISF is similar to that of MDF, that is, there exists some blocking and blurring effects. The filtering performance of FBF is inconspicuous with respect to denoising while slightly affecting the fine structure of the lung. Compared with the original image and filtered images through different baseline methods, the proposed algorithm has a better performance regarding the attenuation of artifacts and/or noise, and the

TABLE I
SNR AND SMIE COMPARISONS FOR THE ORIGINAL AND IMPROVED
IMAGES THROUGH THE PROPOSED ALGORITHM FOR FIGS. 6–8

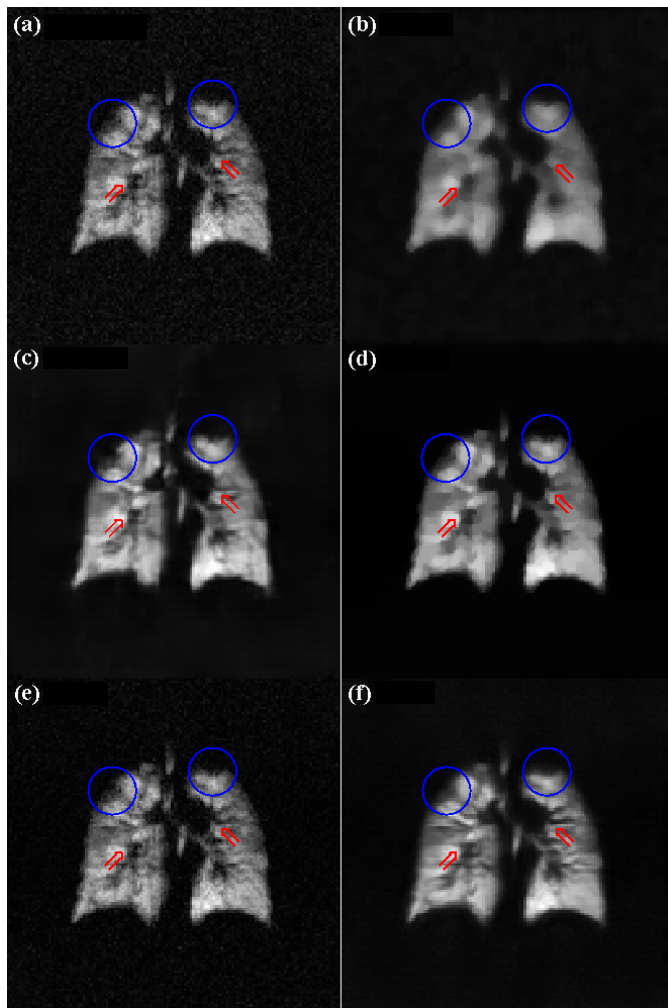|		Fig. 6	Fig. 7	Fig. 8	Average
	Original	10.850	12.764	11.622	11.746
SNR	Our	15.556	18.084	18.175	17.272
	Relative Increment	43.37%	41.68%	56.38%	47.05%
	Original	0.165	0.174	0.178	0.172
SMIE	Our	0.190	0.216	0.212	0.206
	Relative Increment	15.41%	23.86%	19.42%	19.57%

Fig. 7. One slice of the pulmonary HP ^{129}Xe images of the COPD subject (female, 56 years) and the filtered results obtained using different algorithms. (a) Original HP MR image of the sixth layer of the lung. (b)–(f) Filtered results using MDF, BM3D, FISF, FBF, and proposed method. Blue circles: ventilation defects and red arrows: fine structures.

Fig. 8. One slice of pulmonary HP ^{129}Xe images of the asthma subject (female, 34 years) and filtered results obtained using different methods. (a) Original image is filtered through (b)–(f) MDF, BM3D, FISF, FBF, and the proposed algorithm.

protection of details of the HP gas images, which results in an increase in SMIE (see Table I).

For the COPD subject, Fig. 7(a)–(f) shows the original pulmonary HP ^{129}Xe MR image of the sixth layer of the lung, and the filtered results are obtained via MDF, BM3D, FISF, FBF, and proposed algorithm. Blue circles denote the regions of ventilation defects, and red arrows denote the regions of fine structures. Owing to each voxel containing different amounts of airspace (i.e., partial volu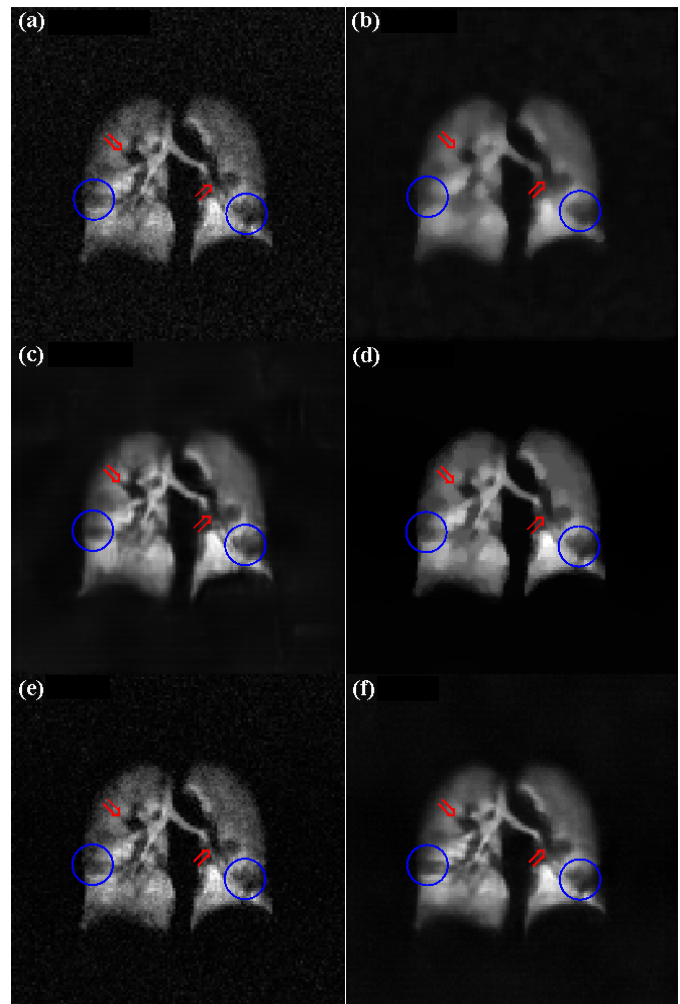me effects) due to the structures of the lung which contains airway, bronchus, bronchioles, vasculature, and alveoli, each of which persists throughout the lung, it is difficult to differentiate in-heterogeneity due to the partial volume effects from artifacts and/or noise. It can be found from Fig. 7 that the original image [viz., Fig. 7(a)] is susceptible to noise/artifacts, and fine details are blurred and/or degenerated because of rapid decline of HP magnetization. It is difficult to directly discern the ROIs, which is unfavorable to understand or distinguish abnormal or normal structures of the lung. After the *k*-space weighting algorithm, the artifacts/noise are effectively eliminated, and fine structures are clearer [see Fig. 7(f)]. This is advantageous to visualize and discriminate ROIs, such as ventilation defects.

Similar to Fig. 6, some blocking artifacts and blurred details are also existed in the filtered results obtained through MDF and FISF [see Fig. 7(b) and (d)]. The BM3D can remove noise and/or artifacts well while slightly degrading the image details [see Fig. 7(c)]. Moreover, we can find that the substantial noise and artifacts linger in Fig. 7(e).

For the asthma subject, Fig. 8(a)–(f) shows an original HP MR image of the fifth layer of the lung, and filtered results obtained using baseline methods and proposed method.

	SNR			SMIE		
	Original	Our	P-value	Original	Our	P-value
Healthy 1	13.141 ±1.574	21.238 ±4.952	0.003	0.155 ±0.014	0.180 ±0.019	0.029
Healthy 2	9.650 ±0.769	6.621 ±2.428	0.002	0.160 ±0.006	0.188 ±0.018	0.021
Healthy 3	7.663 ±0.665	11.780 ±2.612	0.023	0.161 ±0.016	0.184 ±0.013	0.042
COPD	13.042 ±2.512	21.713 ±4.642	0.002	0.162 ±0.012	0.206 ±0.023	0.001
Asthma	12.634 ±1.792	21.168 ±3.065	<0.001	0.168 ±0.015	0.216 ±0.011	<0.001
Total	11.487 ±2.674	18.974 ±5.128	<0.001	0.162 ±0.015	0.193 ±0.021	<0.001

Fig. 9. One slice of a COPD subject and ventilation defect regions. (a) ^{1}H image. (b) ^{1}H segmentation. (c) Original HP ^{129}Xe MR image. (d) Enhanced result of (c) through the proposed method. (e) Registered result of HP and ^{1}H image sets [i.e., (a) and (d)]. (f) Classification of ventilation regions of (d). (g) Determined ventilation defect regions. The VDP values before [i.e., (c)] and after processing [i.e., (d)] are 16.30% and 19.54%.

The meanings of blue circles and red arrows are the same as those in Fig. 7. It can be found that the overall SNR and fine structures of images are improved in Fig. 8(f), and the noise and/or artifacts are mostly eliminated as well. In this case, some ventilation defects and detailed regions (e.g., trachea or vascular) are easily delineated or determined. From Figs. 6–8, the proposed scheme is superior to MDF, BM3D, FISF, and FBF at eliminating disturbances (e.g., artifacts and/or noise) while highlighting fine structures. The same conclusion is also derived from Tables I and II.

Quantitative comparisons are displayed in Table I that lists SNR and SMIE values for the images with and without k-space weighting. Table I indicates that the proposed method not only significantly improve overall SNR but also evidently promote SMIE values.

For the healthy, COPD and asthma subjects, Table II lists the statistical analyses of the SNR and SMIE values for the original and enhanced images obtained using the proposed method. We can see that the P-value in each group of the SNR comparison is smaller than 0.05. This indicates that our method is statistically significantly different from the original for SNR comparisons. It can be also found from Table II that the P-value in each group of SMIE comparison is smaller than 0.05. Thus, the proposed method can improve both SNR and SMIE of HP MR images in a statistical sense. Table II illustrates the better separation between healthy subjects and patients as well.

D. Ventilation Defect Percentage

HP noble gas (^{129}Xe/^{3}He) ventilation-weighted MRI is capable to portray region ventilation patterns in patients with obstructive lung diseases, such as COPD or asthma [35]. When united spatially registered ^{1}H images of the lung, the lung ventilated volume percentage (VVP) and its counterpart ventilation defect percentage (VDP) are recommended quantitative metrics of lung function, where VDP = 1 − VVP [35]. VVP is the ratio of ventilated lung volume in HP gas images to the total lung volume in ^{1}H images. The calculation of VDP/VVP, therefore, needs the determination of ventilation defect regions in HP gas images through the hierarchical k-means clustering
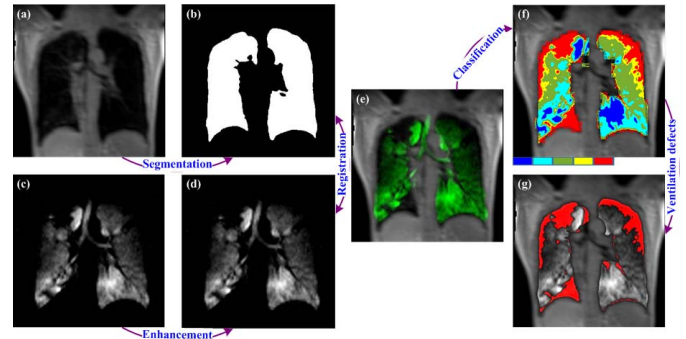
or others, as well as the segmentation of HP and ^{1}H image sets. We adopt the region growing technique to segment the HP and ^{1}H images, and manually exclude the major airways in this section.

One healthy and one COPD subjects are utilized to compare VDP values before and after processing (viz., without or with the proposed k-space-based postprocessing method). The MRI parameters are: TE = 1.9 ms, TR = 4.2 ms, MS = 96 × 84, FOV = 336 × 384 mm^2, ST = 8 mm, BW = 400 kHz, NS = 22, and 3-D bSSFP sequence. The respective FEV$_1$/FVC is 81% and 62%, where FEV$_1$ is the forced expiratory volume in 1 s, and FVC is the forced vital capacity. Fig. 9 displays the 12th slice of COPD subject and determined ventilation defect areas after processing [clusters in Fig. 9(f) represent the gradations of signal intensity or ventilation], where the red color in the image (f) and (g) denotes the ventilation defects. We can see that the ventilation defects are easily delineated. Nevertheless, it is important to note that the segmentation of HP and ^{1}H sets and clustering require much attention because of the lack of ground truth. As for the slice-by-slice VDP values with or without the k-space weighting manipulation (some slices are abandoned because those images are unable to fulfil demands of segmentation or registration), the respective average of VDP before processing is 5.65% and 19.06%, while 5.56% and 20.03% after modulation. Through a Bland–Altman analysis, the mean difference (±SD) between before and after the k-space manipulations is 0.0009 ± 0.0152 L (lower limit = −0.0288 L and upper limit = 0.0307 L) for the healthy volunteer, and −0.0097 ± 0.0175 L (lower limit = −0.0441 L and upper limit = 0.0247 L) for the COPD subject (where SD denotes the standard deviation). Howbeit, the above are the preliminary results for VDP analyses and defects quantification. The separation of healthy and diseased groups, and/or the correlation between the image quantified using the k-space weighting operation and clinical data and patient outcomes, should be further explored.

E. Discussions

A novel postprocessing improvement algorithm is presented to either effectively enhance the SNR or fine details of HP

gas images. Moreover, a new nonreference quality metric called the SMIE is introduced to assess the image quality of HP gas MRI because of the lack of criteria for quantitative evaluation. The algorithm could be attractive to the HP gas community in that it could be applied retrospectively (viz., no additional preparation and cost), and address the specific and well-known sources of image degradation (viz., HP magnetization decay over time due to the repeated RF excitation). The method can be easily actualized by other investigators.

To further increase the sensitivities to diseases or obstructed ventilation, the user can utilize some knowledge of raw data or images (perhaps based on SNR, resolution, or both) to regulate the parameters related to the presented algorithm, such as VDP. The calculation of VDP/VVP requires the segmentation of ^{1}H and HP sets using the region growing, global/local thresholding, k-means clustering, multiple atlas labeling, and fuzzy C-means [36]–[38]. Nevertheless, the k-means clustering possibly fails with some HP gas images that possess low SNR values because of its binary clustering nature and inability to differentiate noise from lung tissue [35]. As stated previously, the enhanced result obtained using the proposed method is a tradeoff between the SNR and fine structures by adjusting parameter α in (9). In this case, we can raise parameter α, to acquire high SNR images to fulfil the demands of k-means clustering. Similarly, one could lessen that parameter, which potentially increases the contrast between regions of normal and obstructed ventilation, to reasonably delineate ventilation defects. Moreover, low SNR is a major limitation for diffusion-weighted imaging [39]. After the proposed method, the overall SNR could be improved, which possibly leads to the improvement of the accuracy regarding diffusion parameter estimation. The above offers more design flexibility for users, making the presented method more general with the aim of satisfying complex or specific requirements for diverse objects and applications.

F. Limitations

There are some limitations to our study. First, the way that the simulation is constructed (taking noisy images and applying artificial HP magnetization decay) potentially alters the noise properties of original ^{1}H images (e.g., water phantom), since applying the artificial magnetization decay possibly artificially down weight the noise as well. Perhaps, it is a good approach that would be taken as a "noiseless" image (i.e., the average of all 100 images), apply the decay weighting and then add random noise. Moreover, the use of simulation experiments seems to provide an opportunity to test the performance over a range of original image quality levels. However, the lack of evidence to show the performance in a very low SNR regime draws the usefulness in that situation into question. In the future, we will explore these arguable issues. Second, the number of subjects in our study is small, especially for patients. Hence, the *in vivo* experimental results provided are insufficient to demonstrate the superiority of the proposed algorithm (specifically for the identification of ventilation defects). In this way, much attention should be paid to the discrimination of ROIs (e.g., ventilation defects or healthy tissue regions) and/or ventilation defect quantification. Third, the need for the performance of image filtering should be framed around the accuracy and precision of ventilation defect identification or other relevant functional ventilation metrics (e.g., PFTs). However, due to the absence of a ground truth, the comparison among diverse established algorithms for HP gas lung ventilation meets many difficulties. This shows a linchpin for our future work. Fourth, the SMIE introduced in this paper requires validation over a very large data set, especially for HP gas MR images. The comparisons between the SMIE and other reference-free metric used in general image processing should be properly manipulated in the further. Fifth, there are some potential negative effects of the proposed k-space-based analysis (Fourier linear filtering in fact), such as the smoothing, noise, or artifacts amplification. In principle, the postprocessing data manipulation should be avoided from happening if possible, since the filtering possibly corrupts raw data/images. However, filtering is important where the improvements in the analytical potential outweigh the potential data corruption. Therefore, the filtering should address specific and well-known sources of image degradation or corruption in traditional HP gas MRI. The findings have potential interests for HP gas MRI community. Finally, the synchronous presentation (the integration of SNR- and resolution-weighted results) possibly generates confusion in the understanding and/or discriminating ROIs (such as some fine structures are potentially masked). We know that HP gas MRI could provide structural and functional information of the lung. If fine details of such information are further highlighted at the same time, the potential of the proposed method will be greatly strengthened.

IV. CONCLUSION

This paper presents an algorithm through the k-space weighting matrices (by implementing the k-space weighting using low-frequency boost and high-frequency modulation which corrects for HP magnetization loss per excitation), and an image fusion process to visually enhance the SNR and fine structural details of HP ^{129}Xe ventilation MR images of the lung. This paper also introduces a second-derivative-like visibility index, reference-free metric (SMIE), to objectively quantify the image quality of pulmonary HP gas MRI. Various metrics (such as SNR, PSNR, SSIM, and SMIE) are applied to compare images reconstructed without or with k-space weighting manipulation. Both simulation and *in vivo* experimental results demonstrate that there are statistically significant differences in both SNR and SMIE terms before and after processing, and the presented method provides improved images (that is, raise SNR and SMIE in HP ^{129}Xe ventilation images, while qualitatively maintaining the appearance of the fine structure and ventilation defects). This is a cost free, intriguing, and promising strategy to improve the image quality (or image augmentation) which can be easily implemented by others, and would be attractive or interesting to the HP gas community. The presented method has the potential to improve the identification, understanding, and/or delineation of ROIs in

the lung, and early detection and/or diagnosis of pulmonary diseases.

REFERENCES

[1] W. Chen *et al.*, "Cancer statistics in China, 2015," *CA: A Cancer J. Clinicians*, vol. 66, no. 2, pp. 115–132, Mar./Apr. 2016.

[2] Q.-Y. Hong *et al.*, "Prevention and management of lung cancer in China," *Cancer*, vol. 121, no. S17, pp. 3080–3088, Sep. 2015.

[3] A. Sodickson *et al.*, "Recurrent CT, cumulative radiation exposure, and associated radiation-induced cancer risks from CT of adults," *Radiology*, vol. 251, no. 1, pp. 175–184, Apr. 2009.

[4] L. Ebner, J. Kammerman, B. Driehuys, M. L. Schiebler, R. V. Cadman, and S. B. Fain, "The role of hyperpolarized ^{129}xenon in MR imaging of pulmonary function," *Eur. J. Radiol.*, vol. 86, pp. 343–352, Jan. 2017.

[5] G. W. Miller, M. Carl, J. F. Mata, G. D. Cates, Jr., and J. P. Mugler, III, "Simulations of short-time diffusivity in lung airspaces and implications for S/V measurements using hyperpolarized-gas MRI," *IEEE Trans. Med. Imag.*, vol. 26, no. 11, pp. 1456–1463, Nov. 2007.

[6] J. F. P. J. Abascal, M. Desco, and J. Parra-Robles, "Incorporation of prior knowledge of signal behavior into the reconstruction to accelerate the acquisition of diffusion MRI data," *IEEE Trans. Med. Imag.*, vol. 37, no. 2, pp. 547–556, Feb. 2018.

[7] N. J. Stewart *et al.*, "Experimental validation of the hyperpolarized ^{129}Xe chemical shift saturation recovery technique in healthy volunteers and subjects with interstitial lung disease," *Magn. Reson. Med.*, vol. 74, no. 1, pp. 196–207, Jul. 2015.

[8] W. W. Ruan *et al.*, "Detection of the mild emphysema by quantification of lung respiratory airways with hyperpolarized xenon diffusion MRI," *J. Magn. Reson. Imag.*, vol. 45, no. 3, pp. 879–888, Mar. 2017.

[9] N. J. Stewart *et al.*, "Reproducibility of quantitative indices of lung function and microstructure from ^{129}Xe chemical shift saturation recovery (CSSR) MR spectroscopy," *Magn. Reson. Med.*, vol. 77, no. 6, pp. 2107–2113, Jun. 2017.

[10] Z. Liu, T. Araki, Y. Okajima, M. Albert, and H. Hatabu, "Pulmonary hyperpolarized noble gas MRI: Recent advances and perspectives in clinical application," *Eur. J. Radiol.*, vol. 83, no. 7, pp. 1282–1291, Jul. 2014.

[11] M. S. Albert *et al.*, "Biological magnetic resonance imaging using laser-polarized ^{129}Xe," *Nature*, vol. 370, no. 6486, pp. 199–201, Jul. 1994.

[12] R. F. Lee, G. Johnson, R. I. Grossman, B. Stoeckel, R. Trampel, and G. McGuinness, "Advantages of parallel imaging in conjunction with hyperpolarized helium—A new approach to MRI of the lung," *Magn. Reson. Imag.*, vol. 55, no. 5, pp. 1132–1141, May 2006.

[13] H. Deng *et al.*, "Constant-variable flip angles for hyperpolarized media MRI," *J. Magn. Reson.*, vol. 263, pp. 92–100, Feb. 2016.

[14] S. Ajraoui, K. J. Lee, M. H. Deppe, S. R. Parnell, J. Parra-Robles, and J. M. Wild, "Compressed sensing in hyperpolarized ^{3}He lung MRI," *Magn. Reson. Med.*, vol. 63, no. 4, pp. 1059–1069, May 2010.

[15] M. He *et al.*, "Dose and pulse sequence considerations for hyperpolarized ^{129}Xe ventilation MRI," *Magn. Reson. Imag.*, vol. 33, no. 7, pp. 877–885, Sep. 2015.

[16] J. Schlemper, J. Caballero, J. V. Hajnal, A. N. Price, and D. Rueckert, "A deep cascade of convolutional neural networks for dynamic MR image reconstruction," *IEEE Trans. Med. Imag.*, vol. 37, no. 2, pp. 491–503, Feb. 2018.

[17] C. Zachiu, M. Ries, C. Moonen, and B. D. de Senneville, "An adaptive non-local-means filter for real-time MR-thermometry," *IEEE Trans. Med. Imag.*, vol. 36, no. 4, pp. 904–916, Apr. 2017.

[18] F. Shi, J. Cheng, L. Wang, P.-T. Yap, and D. Shen, "LRTV: MR image super-resolution with low-rank and total variation regularizations," *IEEE Trans. Med. Imag.*, vol. 34, no. 12, pp. 2459–2466, Dec. 2015.

[19] K. Dabov, A. Foi, V. Katkovnik, and K. Egiazarian, "Image denoising by sparse 3D transform-domain collaborative filtering," *IEEE Trans. Image Process.*, vol. 16, no. 8, pp. 2080–2095, Aug. 2007.

[20] A. Beck and M. Teboulle, "Fast gradient-based algorithms for constrained total variation image denoising and deblurring problems," *IEEE Trans. Image Process.*, vol. 18, no. 11, pp. 2419–2434, Nov. 2009.

[21] K. N. Chaudhury, "Acceleration of the shiftable $O(1)$ algorithm for bilateral filtering and nonlocal means," *IEEE Trans. Image Process.*, vol. 22, no. 4, pp. 1291–1300, Apr. 2013.

[22] H.-H. Chang, C.-Y. Li, and A. H. Gallogly, "Brain MR image restoration using an automatic trilateral filter with GPU-based acceleration," *IEEE Trans. Biomed. Eng.*, vol. 65, no. 2, pp. 400–413, Feb. 2018.

[23] S. Perreault and P. Hebert, "Median filtering in constant time," *IEEE Trans. Image Process.*, vol. 16, no. 9, pp. 2389–2394, Sep. 2007.

[24] R. Q. Xiong *et al.*, "Image denoising via bandwise adaptive modeling and regularization exploiting nonlocal similarity," *IEEE Trans. Image Process.*, vol. 25, no. 12, pp. 5793–5805, Dec. 2016.

[25] J. Cohen-Adad and C. Wheeler-Kingshott, "Quantitative MRI of the spinal cord," in *Single Voxel MR Spectroscopy in the Spinal Cord: Technical Challenges and Clinical Applications*, S. S. Bhavana and D. V. Enrico, Ed. New York, NY, USA: Academic, 2014, pp. 267–290.

[26] J. R. Alger, "Quantitative proton magnetic resonance spectroscopy and spectroscopic imaging of the brain: A didactic review," *Topics Magn. Reson. Imag.*, vol. 21, no. 2, pp. 115–128, Apr. 2010.

[27] L. Zhao *et al.*, "Gradient-Echo Imaging Considerations for Hyperpolarized ^{129}Xe MR," *J. Magn. Reson.*, vol. 113, no. 2, pp. 179–183, Nov. 1996.

[28] S. C. Kale, X. J. Chen, and R. M. Henkelman, "Trading off SNR and resolution in MR images," *NMR Biomed.*, vol. 22, no. 5, pp. 488–494, Jun. 2009.

[29] H. Deng, W. Deng, X. Sun, M. Liu, C. Ye, and X. Zhou, "Mammogram enhancement using intuitionistic fuzzy sets," *IEEE Trans. Biomed. Eng.*, vol. 64, no. 8, pp. 1803–1814, Aug. 2017.

[30] L. Zhao, A. K. Venkatesh, M. S. Albert, and L. P. Panych, "Signal-to-noise ratio comparison of encoding methods for hyperpolarized noble gas MRI," *J. Magn. Reson.*, vol. 148, no. 2, pp. 314–326, Feb. 2001.

[31] Z. Wang, A. C. Bovik, H. R. Sheikh, and E. P. Simoncelli, "Image quality assessment: From error visibility to structural similarity," *IEEE Trans. Image Process.*, vol. 13, no. 4, pp. 600–612, Apr. 2004.

[32] S. Du, L. Cai, Y. Li, and D. Gao, "Model of tip-sample interaction and image reconstruction," *IEEE Trans. Instrum. Meas.*, vol. 55, no. 2, pp. 507–513, Apr. 2006.

[33] B. Zhang, T. Khawaja, R. Patrick, G. Vachtsevanos, M. E. Orchard, and A. Saxena, "Application of blind deconvolution denoising in failure prognosis," *IEEE Trans. Instrum. Meas.*, vol. 58, no. 2, pp. 303–310, Feb. 2009.

[34] S. Ravishankar and Y. Bresler, "MR image reconstruction from highly undersampled k-space data by dictionary learning," *IEEE Trans. Med. Imag.*, vol. 30, no. 5, pp. 1028–1041, May 2011.

[35] P. J. C. Hughes, F. C. Horn, G. J. Collier, A. Biancardi, H. Marshall, and J. M. Wild, "Spatial fuzzy c-means thresholding for semiautomated calculation of percentage lung ventilated volume from hyperpolarized gas and ^{1}H MRI," *J. Magn. Reson. Imag.*, vol. 47, no. 3, pp. 640–646, Mar. 2018.

[36] Y. Yang, Y. Que, S. Huang, and P. Lin, "Multiple visual features measurement with gradient domain guided filtering for multisensor image fusion," *IEEE Trans. Instrum. Meas.*, vol. 66, no. 4, pp. 691–703, Apr. 2017.

[37] K. Hu, X. Gao, and F. Li, "Detection of suspicious lesions by adaptive thresholding based on multiresolution analysis in mammograms," *IEEE Trans. Instrum. Meas.*, vol. 60, no. 2, pp. 462–472, Feb. 2011.

[38] X. Wang, N. D. Georganas, and E. M. Petriu, "Fabric texture analysis using computer vision techniques," *IEEE Trans. Instrum. Meas.*, vol. 60, no. 1, pp. 44–56, Jan. 2011.

[39] F. Lam, S. D. Babacan, J. P. Haldar, M. W. Weiner, N. Schuff, and Z.-P. Liang, "Denoising diffusion-weighted magnitude MR images using rank and edge constraints," *Magn. Reson. Med.*, vol. 71, no. 3, pp. 1272–1284, Oct. 2014.

He Deng received the Ph.D. degree from the Huazhong University of Science and Technology, Wuhan, China.

He is currently an Associate Professor with the Wuhan Institute of Physics and Mathematics, Chinese Academy of Sciences, Wuhan. His current research interests include image processing.
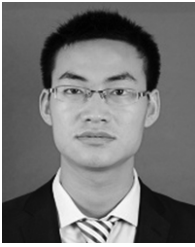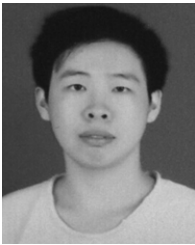
Caohui Duan received the B.S. degree from the Huazhong University of Science and Technology, Wuhan, China, in 2015. He is currently pursuing the Ph.D. degree with the Wuhan Institute of Physics and Mathematics, Chinese Academy of Sciences, Wuhan.

His current research interests include deep learning and image processing.

Huiting Zhang received the M.S. degree from the Wuhan Institute of Physics and Mathematics, Chinese Academy of Sciences, Wuhan, China, in 2007. She is currently pursuing the Ph.D. degree with the Wuhan Institute of Physics and Mathematics, Chinese Academy of Sciences, Wuhan.

Her current research interests include hyperpolarized xenon MRI.

Sa Xiao received the B.E. degree from the Huazhong University of Science and Technology, Wuhan, China, in 2012. He is currently pursuing the Ph.D. degree with the Wuhan Institute of Physics and Mathematics, Chinese Academy of Sciences, Wuhan.

His current research interests include biomedical imaging, compressed sensing, and image processing.

Xianping Sun received the B.S. degree from Peking University, Beijing, China.

He is currently a Professor with the Wuhan Institute of Physics and Mathematics, Chinese Academy of Sciences, Wuhan. His current research interests include signal acquisition and processing.

Junshuai Xie received the B.E. degree from the Huazhong University of Science and Technology, Wuhan, China, in 2013. He is currently pursuing the Ph.D. degree with the Wuhan Institute of Physics and Mathematics, Chinese Academy of Sciences, Wuhan.

His current research interests include hyperpolarized xenon MRI.

Xin Zhou received the Ph.D. degree from the Chinese Academy of Sciences, Wuhan.

He is currently a Professor with the Wuhan Institute of Physics and Mathematics, Chinese Academy of Sciences. His current research interests include scientific developments, imaging acquisition, and data processing.